JKAU: Eng. Sci., **vol. 10 no. 2,** pp. 93-111 (1418 A.H. / 1998 A.D.)

Field Optimization of High Voltage Bushings

M. ABDEL-SALAM* and A. MUFTI**
**Elect. Engng. Dept., King Fahd University, Dhahran*
***Elect. & Comp. Engng. Dept., Faculty of Engineering, King Abdulaziz University, Jeddah, Saudi Arabia*

ABSTRACT. A method is described for optimizing the field stress on HV bushings-penetrating though a flat grounded casing – by modifying their profile, seeking a uniform distribution of the tangential field along the bushing surface. This results in an increase of the inception voltage for surface flashover on the bushing surface. The optimization process was achieved by an algorithm developed for calculating the tangential field component on the bushing surface. The algorithm was based on the charge simulation technique to satisfy the boundary conditions at the electrode, bushing and casing surfaces. The dominant effect in the optimization process is ascribed to the inclination angle and the height of the bushing outside the casing.

1. Introduction

Bushings are used to bring high voltage (HV) conductors through grounded casing, for example, a tank cover of a HV test transformer without excessive electric stresses between the conductor and the edge of the hole in the tank[1]. For voltages ≤ 66 kV, the bushing is no more than a solid insulating material shaped as a tapered cylinder surrounding the HV conductor. The insulating material would withstand the prevailing high field stresses. However, the high tangential components of the field at the interface between the solid insulating material and the surrounding air may cause surface discharges and lead to relatively low flashover voltages.

One solution to the problem is to use special profiles for both the HV conductor and the bushing material[2]. These profiles are shaped to keep the equipotential contours the same as those before introducing the bushing material around the HV conductor. This type of bushings could be manufactured using epoxy resins as the insulating material[3,4].

Another solution to the problem is to design the bushing with an optimized profile where the distribution of the tangential field component would be uniform, thus

increasing the inception voltage of surface flashover, in conformity with HV insulator optimization[5-7]. In this paper, a method is developed for calculating the tangential field component on the bushing surface.

The method developed for calculating the tangential field component along a bushing penetrating through a grounded flat metal plate, which is the tank cover, is based on the charge simulation technique[1,8]. In this technique, lumped charges are used to simulate the surface charge on the bushing, central conductor, top electrode, and tank cover. Generally, lumped charges simulate accurately curved contours than area charges[5,6] which approximate the contour by straight-line segments.

First, the proposed method for calculating the tangential field is explained. Then, the procedure of optimization is discussed, where some parameters that describe the bushing profile are modified to achieve acceptable degree of field uniformity. Finally, the optimized profiles are discussed in terms of the geometrical parameters of the bushing.

2. Method of Analysis

2.1 Bushing Geometry

Figure 1 shows a bushing penetrating through a grounded flat metal plate, which is the tank cover of a HV test transformer. The profile of the arrangement in Fig. 1 is defined by the inclination angle α, the heights H_1 and H_2 outside and inside the tank, and the base radius R_b of the bushing, in addition to the central conductor radius R_c inside the bushing and the radius R_e of the top electrode outside the bushing. This is in conformity with the profile shapes adopted by some bushing manufacturers[9].

2.1.1 The Top Electrode

The r- and z-coordinates of N_e contour points selected on the top electrode are expressed as (Fig. 1).

$$r(i) = \sqrt{i.\Delta z(2R_e - i.\Delta z)}\,; \quad i = 1,2,...,N_e \tag{1}$$

$$z(i) = H_1 + i.\Delta z_1\,; \quad i = 1,2,...,N_e \tag{2}$$

where $\Delta z_1 = \dfrac{2R_e}{N_e + 1}$ and H_1 is the height of the bushing outside the tank (Fig. 1).

In Eq. (2), the contour points on the top electrode are spaced equally along the z-direction.

2.1.2 The Central Conductor

The r- and z-coordinates of N_c contour points selected on the central conductor are expressed as (Fig. 1).

$$r(i) = R_c \quad ; i = N_e + 1, N_e + 2, ..., N_e + N_c \tag{3}$$

$$z(i) = H_1 - \Delta z_i \quad ; i = N_e + 1, N_e + 2, ..., N_e + N_c \tag{4}$$

where $\Delta z_i = \dfrac{L_c(\lambda_1 - 1)\left(\lambda_1^{i-N_e} - 1\right)}{\lambda_1^{N_c} - 1}$ and $\lambda_1 > 1$.

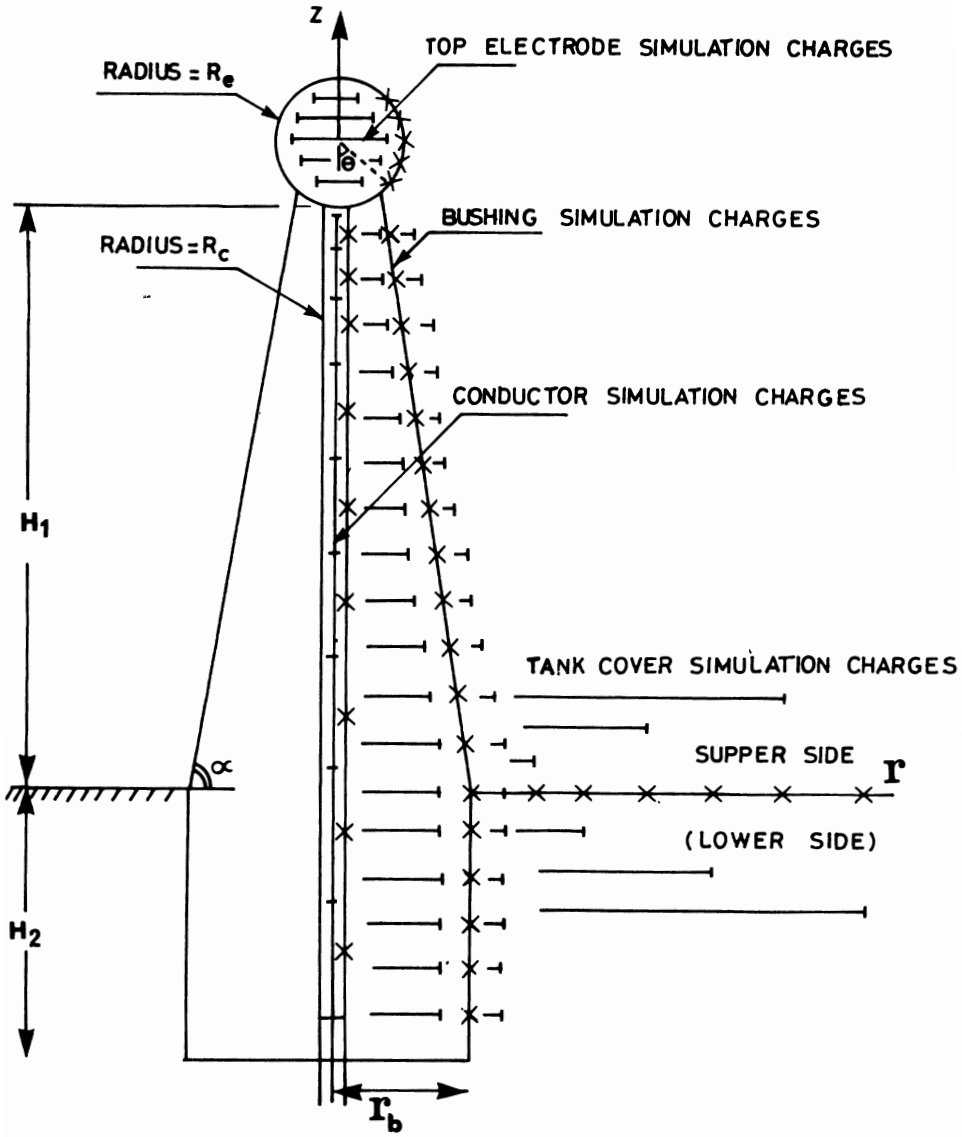

FIG. 1. Charge representation of a bushing penetrating through a grounded flat plane.

In Eq. (4), the contour points on the central conductor of length L_c are not spaced equally along the z-direction. The spacing between the points is small near the top electrode and increases gradually in the direction away from the electrode. Of the contour points N_{c1} points are outside the tank and $N_{c2}(= N_c - N_{c1})$ points are inside the tank.

2.1.3 The Bushing

a) Tapered Party

The r- and z-coordinates of N_{b1} contour points selected on the bushing surface outside the tank are expressed as (Fig. 1).

$$r(i) = R_b - \frac{H_1 - z(i)}{\tan\alpha} \quad ; i = N_e + N_c + 1, N_e + N_c + 2, ..., N_e + N_c + N_{b1} \tag{5}$$

$$z(i) = (i - N_e - N_c).\Delta z_2 \; ; i = N_e + N_c + 1, N_e + N_c + 2, ..., N_e + N_c + N_{b1} \tag{6}$$

where $\Delta z_2 = \frac{H_1}{N_{b1} + 1}$ and R_b is the base radius of the bushing (= radius of the cylindrical portion of the bushing), Fig. 1.

In Eq. (6), the contour points on the tapered part of the bushing are spaced equally along the z-direction.

c) Cylindrical Part

The r- and z-coordinates of N_{b2} contour points selected on the bushing surface inside the tank are expressed as (Fig. 1).

$$r(i) = R_b; \; i = N_e + N_c + N_{b1} + 1, N_e + N_c + N_{b1} + 2, ..., N_e + N_c + N_b \tag{7}$$

$$z(i) = -H_2 + (i - N_e - N_c - N_{b1}).\Delta z_3; i = N_e + N_c + N_{b1} + 1, \; N_e + N_c + N_{b1} + 2, ..., N_e + N_c + N_b \tag{8}$$

where

$$\Delta z_3 = \frac{H_2}{N_{b1} + 1} \text{ and } N_b = N_{b1} + N_{b2}$$

In Eq. (8), the contour points on the cylindrical part of the bushing are spaced equally along the z-direction.

2.1.4 The Tank Cover

The r- and z-coordinates of N_t contour points selected on the tank cover are expressed as, (Fig. 1).

$$r(i) = R_b + R_b \lambda_2^{i - N_e - N_c - N_b}; \; i = N_e + N_c + N_b + 1, \; N_e + N_c + N_b + 2, ..., N_e + N_c + N_b + N_t \tag{9}$$

$$z(i) = 0.0; \; i = N_e + N_c + N_b + 1, N_e + N_c + N_b + 2, ..., N_e + N_c + N_b + N_t \tag{10}$$

where $\lambda_2 > 1$.

In Eq. (10), the contour points on the tank cover are not spaced equally along the r-direction. The spacing between the points is small near the bushing and increases gradually in the direction away from the bushing.

2.2 Surface Charge Simulation

2.2.1 The Top Electrode

Due to the axial symmetry of the arrangement, Fig. 1, the surface charge on the top electrode is simulated by N_e fictitious ring charges whose z-coordinates ($Z(j)=z(j)$, $j = 1,2,...,N_e$) are the same as the selected contour points on the electrode. The radii $R(i)$ of the ring charges are expressed in terms of the r-coordinates of the contour points (Fig. 1).

$$R(j) = \beta_1 r(j);\ j = 1,2,...,N_e \tag{11}$$

where β_1 is a fraction ranging from 0.2 to 0.5 for acceptable accuracy of the simulation.

2.2.2 The Central Conductor

The surface charge on the central conductor is simulated by N_c fictitious ring charges, whose z-coordinates ($Z(j) = z(j), j = N_e + 1, N_e + 2,...,N_e + N_c$) are the same as the selected contour points on the conductor. The radii $R(i)$ of the ring charges are expressed in terms of the r-coordinates of the contour points (Fig. 1).

$$R(j) = \beta_2 r(j);\ j = N_e + 1, N_e + 2,..., N_e + N_c \tag{12}$$

where β_2 is a fraction ranging from 0.2 to 0.5 for acceptable accuracy of the simulation.

2.2.3 The Bushing

In the bushing of dielectric constant ε_r, dipoles are aligned by the applied electric field and compensate for each other through the volume of the insulator, leaving net charges only on the surface. These charges are simulated by fictitious lumped ring charges in the bushing volume and in the surrounding air to match the axial symmetry of the arrangement. The number of simulation charges in the insulator is $N_i(=N_b)$, the same as that in air, N_a. The z-coordinates of simulation charges either in air or in bushing ($Z(j) = z(j);j = N_e + N_c + 1, N_e + N_c + 2,...,N_e + N_c + N_b$) are the same as the selected contour points on the bushing profile. Thus, the z-coordinate $Z(j)$ for rings in air are the same as those in the bushing. The radii $R(i)$ of the ring charges in bushing are expressed in terms of the r-coordinates of the contour points (Fig. 1).

$$R(j) = \beta_3 r(j);\ j = N_e + N_c + 1, N_e + N_c + 2,..., N_e + N_c + N_b \tag{13}$$

where β_3 is a fraction ranging from 0.4 to 0.6 for acceptable accuracy of the simulation.

The radii $R(i)$ of the ring charges in air are expressed in terms of the r-coordinates of the contour points (Fig. 1).

$$R(j) = \beta_4 r(j - N_b);\ j = N_e + N_c + N_b + 1, N_e + N_c + N_b + 2,..., N_e + N_c + 2N_b \tag{14}$$

where β_4 is a factor ranging from 1.2 to 1.7 for acceptable accuracy of the simulation.

2.2.4 The Tank Cover

As the tank cover is usually grounded, it is charged due to the voltage applied to the central conductor. The surface charge on each side of the cover is simulated by two sets of ring charges, N_{t1} and N_{t2}, respectively as shown in Fig. 1. The radii of the N_{t1} ring charges simulating the upper side of the tank cover are expressed in terms of the r-coor-

dinates of contour points selected on the tank cover as (Fig. 1).

$$R(j) = r(j - N_b);\ j = N_e + N_c + 2N_b + 1, N_e + N_c + 2N_b + 3, \ldots, N_e + N_c + 2N_b + N_t \quad (15)$$

The z-coordinates of the N_{t1} charges simulating the upper side of the tank cover are expressed as

$$Z(j) = R(j) - R_b;\ j = N_e + N_c + 2N_b + 1, N_e + N_c + 2N_b + 3, \ldots, N_e + N_c + 2N_b + N_t \quad (16)$$

The radii of the N_{t2} ring charges simulating the lower side of the tank cover are expressed in terms of the r-coordinates of contour points selected on the tank cover as (Fig. 1).

$$R(j) = r(j - N_b);\ j = N_e + N_c + 2N_b + N_{t1} + 2, \quad N_e + N_c + 2N_b + N_{t1} + 4, \ldots, N_e + N_c + 2N_b + N_t \quad (17)$$

where $N_t = N_{t1} + N_{t2}$.

The z-coordinates of the N_{t2} charges simulating the lower side of the tank cover are expressed as

$$Z(j) = -(R(j) - R_b);\ j = N_e + N_c + 2N_b + N_{t1} + 2, \quad N_e + N_c + 2N_b + N_{t1} + 4, \ldots, N_e + N_c + 2N_b + N_t \quad (18)$$

In Eq. (15) and (17), the radial coordinates of the contour points expressed by Eq. (9) are equal to those of the ring charges simulating the tank's upper-side and lower-side alternately.

2.3 Electric Potential Equations

2.3.1 At the Top Electrode Surface

The potential $\phi_1(r, z)$ at any point (r, z) on the electrode/air boundary is the algebraic sum of the potentials at this point, produced by the ring charges belonging to the top electrode, the conductor, the bushing and the lower side of the tank cover (Eq. (1.1) in Appendix 1).

2.3.2 At the Central Conductor/Bushing Interface

The potential $\phi_{2o}(r, z)$ at any point (r, z) on the central conductor/bushing boundary outside the tank is the algebraic sum of the potentials at this point, produced by the ring charges belonging to the top electrode, the conductor, the air and the lower side of the tank cover (Eq. (1.2) in Appendix 1).

Also, the potential $\phi_{2i}(r, z)$ at any point (r, z) on the central conductor/bushing boundary inside the tank is the algebraic sum of the potentials at this point, produced by the ring charges belonging to the top electrode, the conductor, the air and the upper side of the tank cover (Eq. (1.3) in Appendix 1).

2.3.3 At the Bushing Surface

The potential $\phi_{3ob}(r, z)$ at any point (r, z) along the bushing surface outside the tank is the algebraic sum of the potentials at this point, produced by the ring charges belong-

ing to the top electrode, the conductor, the air and the lower side of the tank cover if the point is seen from the bushing side (Eq. (1.4) in Appendix 1). If the point is seen from the air side, the potential $\phi_{3oa}(r, z)$ is the algebraic sum of the potentials at this point, produced by the ring charges belonging to the top electrode, the conductor, the bushing and the lower side of the tank cover (Eq. (1.5) in Appendix 1).

The potential $\phi_{3ib}(r, z)$ at any point (r, z) along the bushing surface inside the tank is the algebraic sum of the potentials at this point, produced by the ring charges belonging to the top electrode, the conductor, the air and the upper side of the tank cover if the point is seen from the bushing side (Eq. (1.6) in Appendix 1). If the point is seen from the air side, the potential ϕ_{3ia} (r, z) is the algebraic sum of the potentials at this point, produced by the ring charges belonging to the top electrode, the conductor, the bushing and the upper side of the tank cover (Eq. (1.7) in Appendix 1).

2.3.4 At the Tank Cover

The potential $\phi_{4o}(r, z)$ at any point (r, z) along the surface of the tank cover is the algebraic sum of the potentials at this point, produced by the ring charges belonging to the top electrode, the conductor, the bushing and the lower side of the tank cover if the point is seen from outside the tank (Eq. (1.8) in Appendix 1).

The potential $\phi_{4i}(r, z)$ at any point (r, z) along the surface of the tank cover is the algebraic sum of the potentials at this point, produced by the ring charges belonging to the top electrode, the conductor, the bushing and the upper side of the tank cover if the point is seen from inside the tank (Eq. (1.9) in Appendix 1).

2.4 Electric Field Equations

2.4.1. At the Bushing Surface

The normal electric field $E_{noa}(r, z)$ at any point (r, z) along the bushing surface outside the tank is the vector sum of the normal field components at this point due to the ring charges belonging to the top electrode, the conductor, the bushing and the lower side of the tank cover if the point is seen from the air side (Eq. 2.1 in Appendix 2). If the point is seen from the bushing side, the normal electric field $E_{nob}(r, z)$ is the vector sum of the normal field components due to the ring charges belonging to the top electrode, the conductor, the air and the lower side of the tank cover (Eq. 2.2 in Appendix 2).

The normal electric field $E_{nia}(r, z)$ at any point (r, z) along the bushing surface inside the tank is the vector sum of the normal field components at this point due to the ring charges belonging to the top electrode, the conductor, the bushing and the upper side of the tank cover if the point is seen from the air side (Eq. 2.3 in Appendix 2). If the point is seen from the bushing side, the normal electric field $E_{nib}(r, z)$ is the vector sum of the normal field components due to the ring charges belonging to the top electrode, the conductor, the air and the upper side of the tank cover (Eq. 2.4 in Appendix 2).

2.5 Boundary Conditions and Defining Equations

2.5.1 At the Top Electrode Boundary

a) The potential $\phi_1(r, z)$ calculated by Eq. (1.1) at every point on the electrode surface is equal to the applied voltage V, *i.e.*,

$$\phi_1(r, z) = V \tag{19}$$

2.5.2 At the Central Conductor Boundary

a) The potential $\phi_{2o}(r, z)$ calculated by Eq. (1.2) at every point on the surface of the central conductor outside the tank is equal to the applied voltage V; *i.e.*,

$$\phi_{2o}(r, z) = V \tag{20}$$

b) The potential $\phi_{2i}(r, z)$ calculated by Eq. (1.3) at every point on the surface of the central conductor inside the tank is equal to the applied voltage V; *i.e.*,

$$\phi_{2i}(r, z) = V \tag{21}$$

2.5.3 At the Bushing Boundary

a) The potential $\phi_{3ob}(r, z)$ calculated by Eq. (1.4) at every point on the bushing surface outside the tank when seen from the bushing side is equal to the potential $\phi_{3oa}(r, z)$ calculated by Eq. (1.5) when the point seen from the air side; *i.e.*,

$$\phi_{3ob}(r, z) = \phi_{3oa}(r, z) \tag{22}$$

b) The potential $\phi_{3ib}(r, z)$ calculated by Eq. (1.6) at every point on the bushing surface inside the tank when seen from the bushing side is equal to the potential $\phi_{3ia}(r, z)$ calculated by Eq. (1.7) when the point seen from the air side; *i.e.*,

$$\phi_{3ib}(r, z) = \phi_{3ia}(r, z) \tag{23}$$

c) The normal field components $E_{noa}(r, z)$ and $E_{nob}(r, z)$ in the air and in the bushing at any point on the bushing surface outside the tank, calculated by Eq. (2.1) and (2.2) respectively, are related through the relative permittivity of the bushing ε_r; *i.e.*,

$$E_{noa}(r, z) = \varepsilon_r E_{nob}(r, z) \tag{24}$$

d) The normal field components $E_{nia}(r, z)$ and $E_{nib}(r, z)$ in the air and in the bushing at any point on the bushing surface inside the tank, calculated by Eq. (2.3) and (2.4) respectively, are related through the relative permittivity of the bushing, ε_r; *i.e.*,

$$E_{nia}(r, z) = \varepsilon_r E_{nib}(r, z) \tag{25}$$

2.5.4 At the Tank Cover

a) The potential $\phi_{4o}(r, z)$ calculated by Eq. (1.8) at every point on the surface of the tank cover seen from outside is equal to 0.0; *i.e.*,

$$\phi_{4o}(r, z) = 0.0 \tag{26}$$

b) The potential $\phi_{4i}(r, z)$ calculated by Eq. (1.9) at every point on the surface of the tank cover seen from outside is equal to 0.0, *i.e.*,

$$\phi_{4i}(r, z) = 0.0 \tag{27}$$

2.6 Determination of Simulation Charges

Satisfaction of pertaining boundary conditions at the top electrode, the central conductor, the bushing profile and the grounded tank cover formulates a set of simultaneous equations whose solution determines the magnitudes of the unknown simulation charges. This is described in detail as follows.

Satisfaction of the boundary condition expressed by Eq. (19) at the N_e selected con-

tour points on the electrode surface, the boundary condition expressed by Eq. (20) at the N_{c1} points selected on the conductor surface outside the tank, the boundary condition expressed by Eq. (21) at the N_{c2} points selected on the conductor surface inside the tank, the boundary condition expressed by Eq. (22) at the N_{b1} points selected on the bushing surface outside the tank, the boundary condition expressed by Eq. (23) at the N_{b2} points selected on the bushing surface inside the tank, the boundary condition expressed by Eq. (24) at the N_{b1} points selected on the bushing surface outside the tank, the boundary condition expressed by Eq. (25) at the N_{b2} points selected on the bushing surface inside the tank and the boundary conditions expressed by Eq. (26) and (27) at the N_t points selected on the tank surface results in a set of equations whose solution determines the unknown simulation charges. The matrix defining this set of equations is shown in Fig. 2.

Once the simulation charges are determined, the potential distribution along the bushing surface is determined using Eq. (1.5) and (1.7) in Appendix 1. Also, the electric field components along the bushing profile are obtained. Of course, the tangential field at any point is the slope of the potential distribution along the bushing surface outside the tank and is obtained directly using Eq. (3.1) in Appendix 3.

2.7 Bushing Optimization

The procedure adopted for optimizing the bushing profile is to search for the slope angle α, which results in an almost uniform distribution of the tangential field over the bushing surface for given values of R_e, R_c, R_b, H_1 and H_2. The effect of the bushing geometry represented by R_e, R_c, R_b and H_1 in addition to the relative permittivity ε_r of the bushing material on the optimized dimensions of the profile is discussed.

3. Results and Discussion

3.1 Accuracy of Simulation

In the charge simulation technique, the number of boundary points is equal to the number of unknowns. The matrix defining the set of equations describing the boundary conditions has numerous zero terms as shown in Fig. 2. Subsequently, the matrix has a wide variation in its elements ranging from very high values to zero values. This reflects itself in the "matrix condition", when solved by Gauss or Crout decomposition technique[10]. The condition of the matrix was found better for the straight profiles investigated here than the case for curved profiles[7].

The values of the unknown charges satisfy the boundary conditions in an acceptable manner, only with a careful choice of both the number of simulation charges and the coordinates of these charges. Therefore, the simulation accuracy depends strongly on the assumptions concerning the simulation charges in both number and coordinates[7]. For straight profiles, the choice of the coordinates is systematic according to Eq. (1-10). The number of simulation charges is obtained through several attempts starting at first with small number of simulation charges until the simulation accuracy becomes satisfactory. This is in conformity with previous findings, where the increase in the number of simulation charges leads sometimes to bad conditioning of solutions instead of producing better accuracy for a single dielectric geometry[11].

Simulation charge / Contour point		Top electrode	Central conductor	Bushing surface		Tank cover	
				air side	bushing side	upper side	lower side
On top electrode Eq. (19)				zero		zero	
On central electrode	Eq. (20)				zero	zero	
	Eq. (21)				zero		zero
On bushing surface	Eq. (22)				zero	zero	
	Eq. (23)			zero		zero	
	Eq. (24)				zero		zero
	Eq. (25)			zero			zero
On tank cover	Eq. (26)			zero		zero	
	Eq. (27)			zero			zero

FIG. 2. Zero terms of the matrix defined by Equations 19-27.

For the investigated geometry, the number of simulation charges N_e, N_c, N_{b1}, N_{b2}, N_{t1}, and N_{t2} are chosen equal to 8, 24, 12, 4, 10 and 10 respectively.

While one boundary condition is to be satisfied over the surface of the central conductor, there are two boundary conditions for the bushing surface. In other words, the number of equations written per point on the bushing surface is double that for a point on the conductor surface. This is why the number of boundary points on the bushing surface is chosen smaller than the number of boundary points on the central conductor.

Consider the geometry shown in Fig. 1 whose dimensions are: $R_e = 20$ mm, $R_c = 3.75$mm, $H_1 = 300$ mm, $H_2 = 100$ mm and $\varepsilon_r = 3$. The value of R_b is directly determined by the following equation.

$$R_b = R_e \sin\theta + \{ R_e(1 - \cos\theta) + H_1 \} / \tan\alpha \tag{28}$$

where θ is the angle defining the intersection of the bushing profile with the top electrode as shown in Fig. 1.

Figure 3 shows computer results for the potential distribution along the bushing surface. At each point outside the tank, the potential is calculated when the point is seen from the air side $\phi_{3oa}(r, z)$ and when seen from the bushing side $\phi_{3ob}(r, z)$. Also, at each point inside the tank, the potential is calculated when the point is seen from the air side $\phi_{3ia}(r, z)$ and when seen from the bushing side $\phi_{3ib}(r, z)$. It is very satisfying to observe the precise equality of $\phi_{3oa}(r, z)$ and $\phi_{3ob}(r, z)$ outside the tank and of $\phi_{3ia}(r, z)$ and $\phi_{3ib}(r, z)$ inside the tank, which differed by less than 1%. This indicates the accuracy of the proposed simulation technique.

The calculated potentials satisfy not only the boundary conditions on the bushing surface, but also the boundary condition on the top electrode and the central conductor, where the deviation from the applied voltage V did not exceed 0.6%.

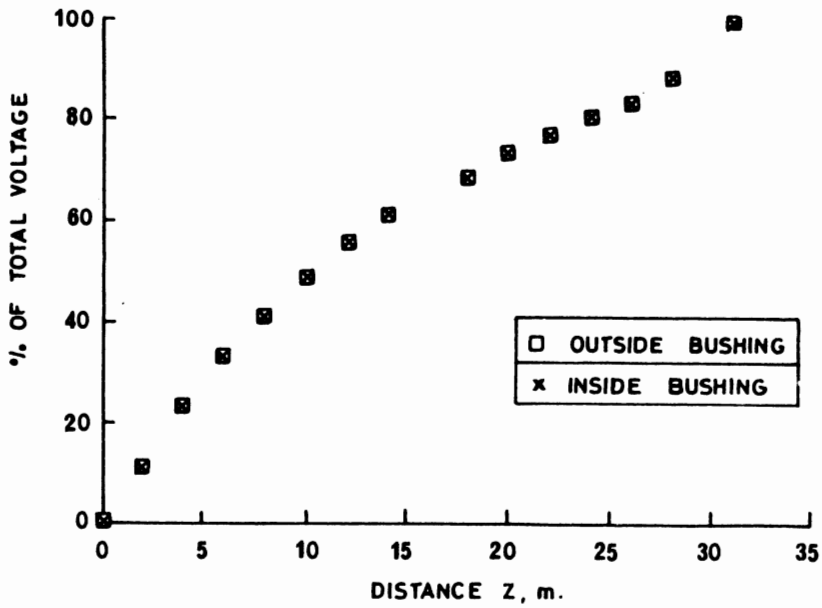

FIG. 3. Potential distribution along the bushing surface ($\varepsilon_r = 3$, $\alpha = 80°$, $H_1 = 300$ mm, $R_e = 20$ mm, $R_c = 3.75$ mm, $\theta = 45°$)

Of course, the accuracy of the potential calculation along the bushing surface reflects itself in the accuracy of the predicted values of the tangential field component.

3.2 Bushing Optimization

To optimize the shape of the bushing, the effects of changing its geometry represented by α, R_e, R_c, R_b and H_1 as well as the relative permittivity ε_r on the tangential field distribution along the bushing surface are studied. Of course, changing the angle θ results in a change of R_b for the same values of α, R_e and H_1 in conformity of Eq. (28).

Figure 4 shows the potential distribution along the bushing surface for different inclination angles. It is quite clear that the tangential field for non-optimized bushing is high near the top electrode and tank cover. Such high field intensity may be the origin of flashover on the bushing surface. On the other hand, the field is almost uniform along the optimized bushing, which makes the probability of flashover on the bushing lower for the same applied voltage.

Changing the inclination angle α from 66° to 90° results in varying the potential distribution along the bushing surface as shown in Fig. 5. The optimal value of α is between 68° and 72°, where the potential distribution is almost linear and hence the tangential field along the insulator surface is almost uniform.

As shown in Fig. 4., the line integral of the tangential field along the bushing surface *equals the applied voltage for* both the optimized and non-optimized profiles. This is also a measure of the accuracy of the proposed simulation technique.

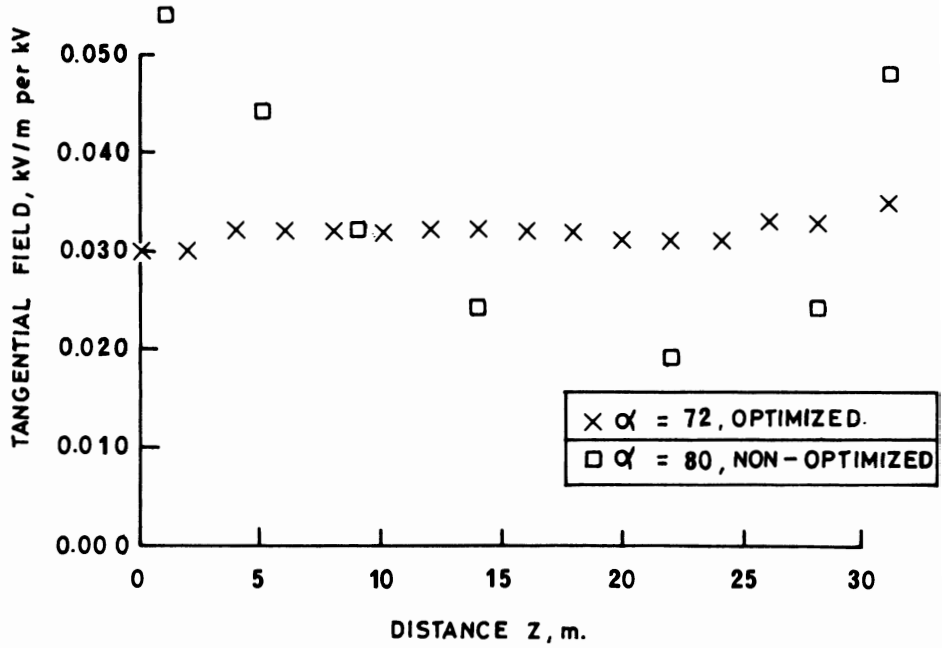

FIG. 4. Tangential field distribution along the profile for optimized and non-optimized bushings ($\varepsilon_r = 3$. $H_1 = 300$ mm, $R_e = 20$ mm, $R_c = 3.75$ mm, $\theta = 45°$).

Figure 6 shows the effect of changing the relative permittivity of the bushing material on the potential distribution. The higher the relative permittivity the smaller the tangential field near the top electrode with minor influence on the field value near the tank cover. The optimal value of ε_r lies between 3 and 4 for the geometry chosen for the bushing, where the surface potential distribution is almost linear.

Figures 7 and 8 show, respectively, the effect of the radius of the top electrode R_e and the radius of the central conductor R_c on the whole potential distribution. As is well known, the larger the radius R_e the smaller the rate of change of field in its vicinity in conformity with the potential distribution shown in Fig. 7. The smaller the conductor radius R_c the higher is the field nonuniformity along the bushing surface, Fig. 8.

Figures 9 and 10 show the potential distribution along the bushing surface for $H_1 = 0.2$ m and 0.6 m, respectively. The optimal value of α, which results in almost uniform distribution of the tangential field, is almost the same irrespective of the value of H_1.

3.3 Tangential Field Similarity

One of the questions which faces the design engineer is related to how the dimensions of the bushing will affect the simulation procedure and its accuracy.

For voltages ≤ 66 kV, the dimensions of outdoor bushings may reach a meter, while those for indoor applications may be a few decimeters. The dimensions of the bushings also change widely with the voltage rating. Similarly, the size of the top electrode

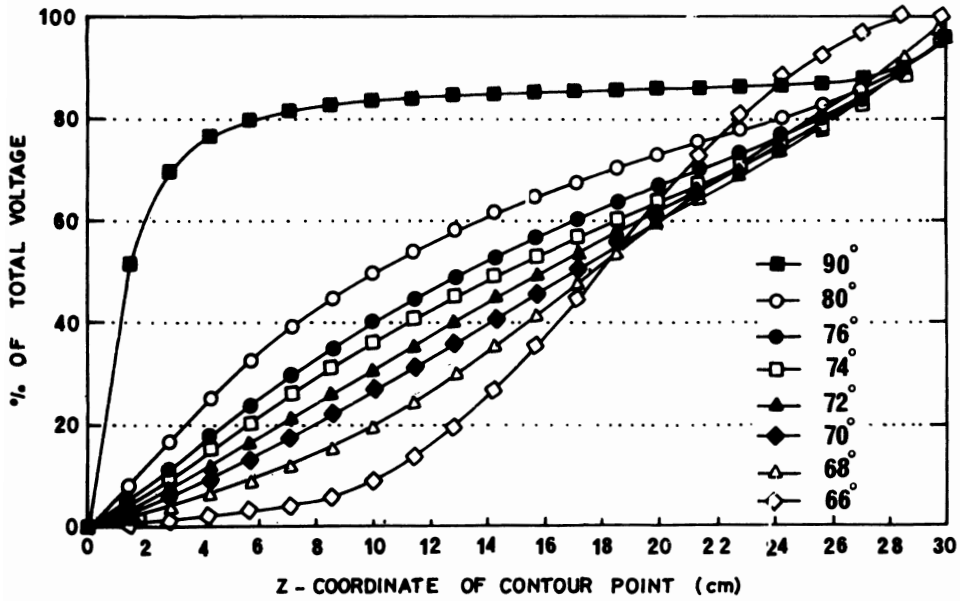

FIG. 5. Potential distribution along the bushing surface for different values of α ($\varepsilon_r = 3$, $H_1 = 300$ mm, $R_e = 20$ mm, $R_c = 3.75$ mm, $\theta = 45°$).

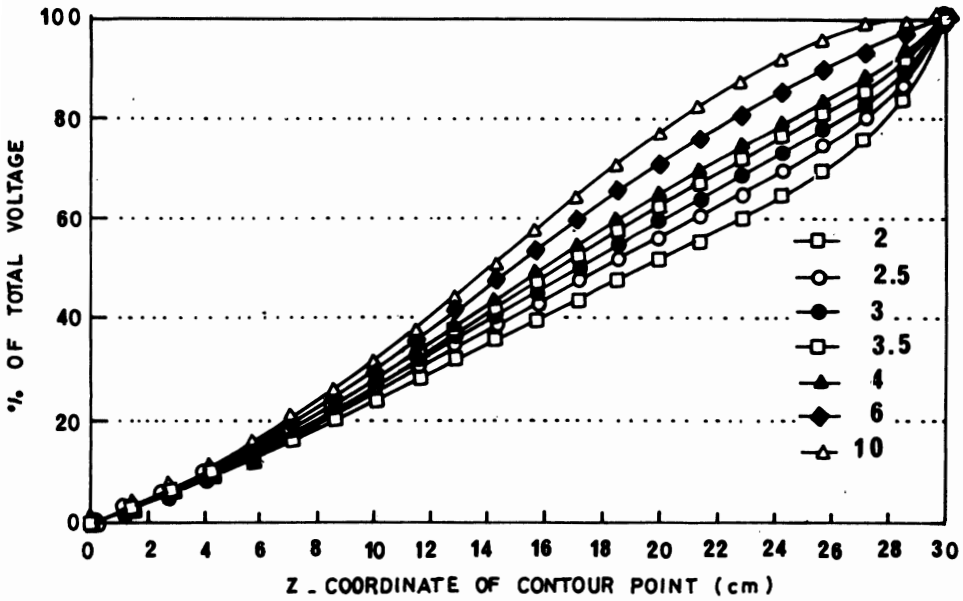

FIG. 6. Potential distribution along the bushing surface for different values of ε_r ($\alpha = 70°$, $H_1 = 300$ mm, $R_e = 20$ mm, $R_c = 3.75$ mm, $\theta = 45°$).

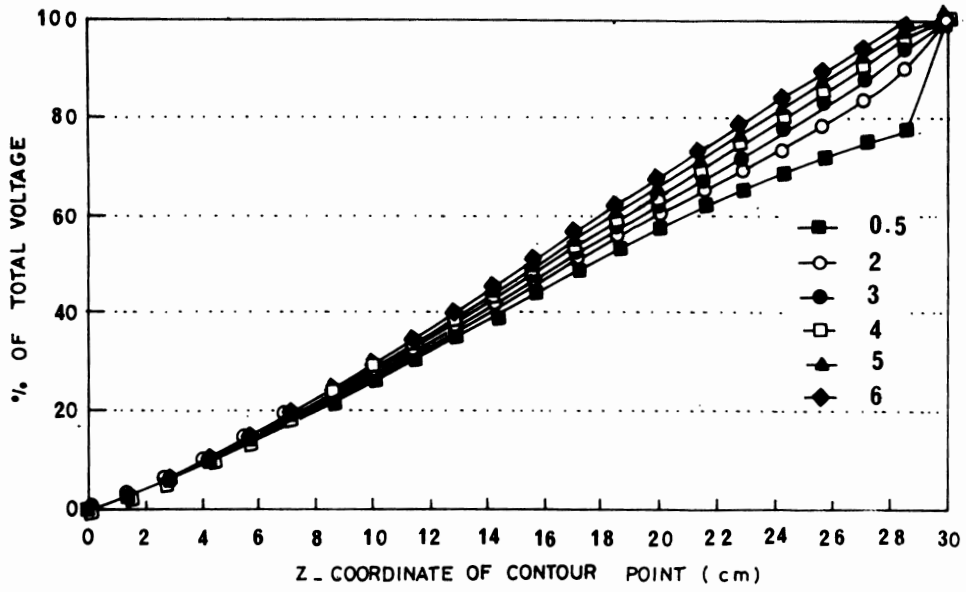

FIG. 7. Potential distribution along the bushing surface for different values of R_e ($\varepsilon_r = 3$, $\alpha = 70°$, $H_1 = 300$ mm, $R_c = 3.75$ mm, $\theta = 45°$).

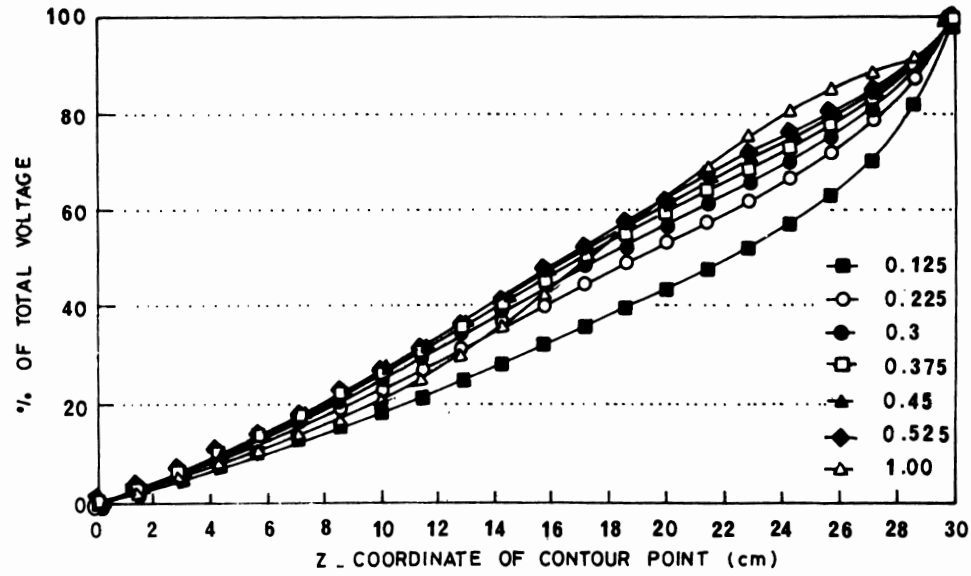

FIG. 8. Potential distribution along the bushing surface for different values of R_c ($\varepsilon_r = 3$, $\alpha = 70°$, $H_1 = 300$ mm, $R_e = 20$ mm, $\theta = 45°$).

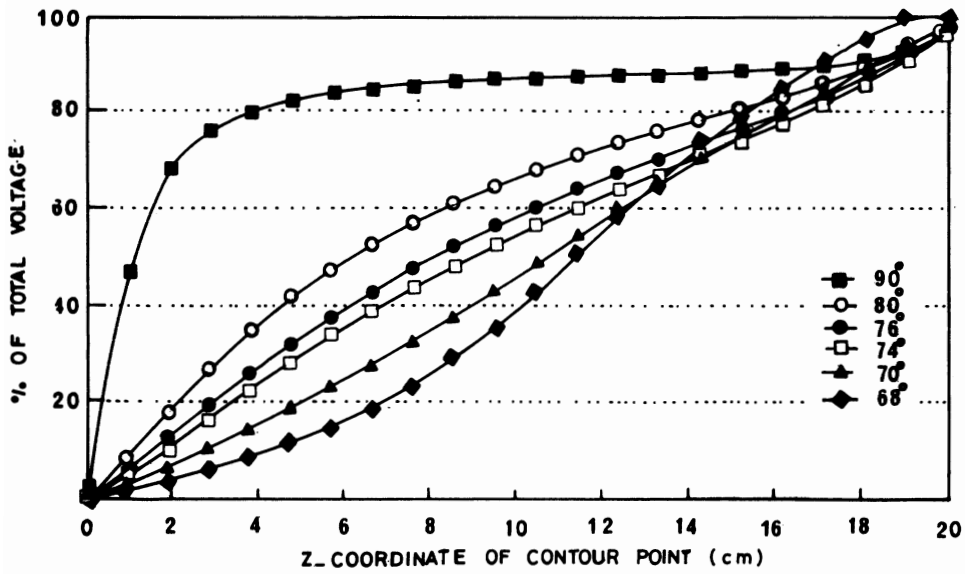

FIG. 9. Potential distribution along the bushing surface for different values of α ($\varepsilon_r = 3$, $H_1 = 200$ mm, $R_e = 20$ mm, $R_c = 3.75$ mm, $\theta = 45°$).

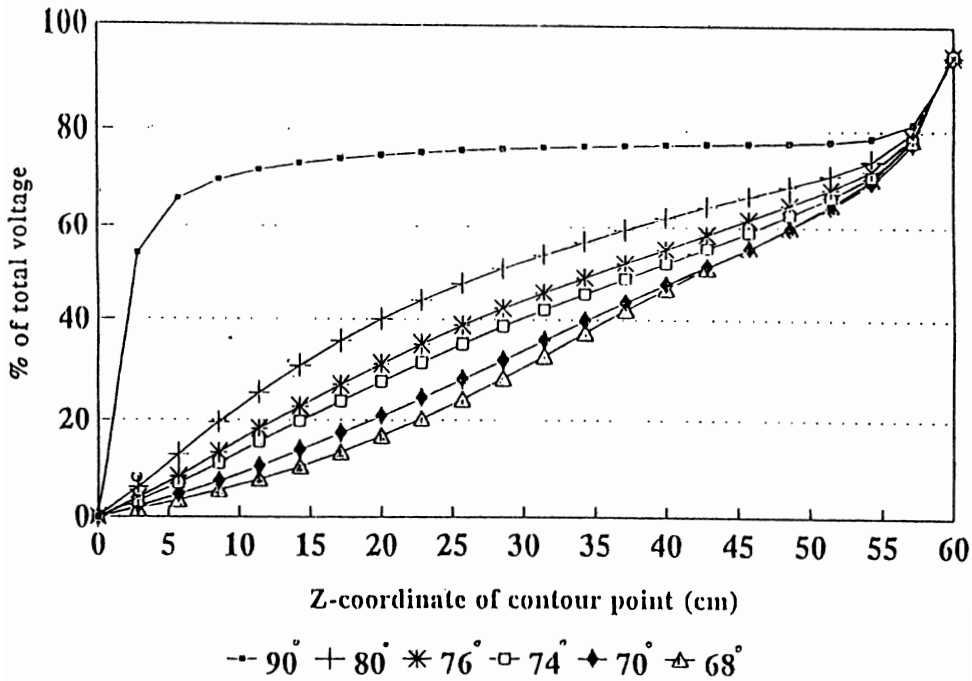

FIG. 10. Potential distribution along the bushing surface for different values of α ($\varepsilon_r = 3$, $H_1 = 600$ mm, $R_e = 20$ mm, $R_c = 3.75$ mm, $\theta = 45°$).

increases with the applied voltage to keep it free from corona discharges. Inspection of the defining equations, outlined before, shows that a field-similarity does exist for electrostatic fields, *i.e.*, field without space charge. In other words, the dimensions of a given bushing when scaled-down by a specific ratio, the per-unit tangential field distribution when referred to the peak value remains the same. The absolute values of the field for the original bushing are those for the scaled-down case after being, also scaled-down by the same ratio. This is very helpful for the proposed simulation technique, as a big bushing can be treated through an equivalent small one, where a reasonably large number of boundary points results in a satisfactory matching of the boundary conditions over the surfaces involved in the bushing[7].

Conclusion

An approach is suggested to optimize the profile of HV bushings to have a uniform tangential field distribution over their surface. The dominant effect in the optimization process is ascribed to the inclination angle of the tapered part and the height of the bushing outside the tank. On the other hand, the conductor radius, the top-electrode radius, the bushing height outside the tank and the permittivity of the bushing material have moderate effects on the tangential field distribution.

Acknowledgement

The authors wish to acknowledge their respective universities for the support they received during the progress of this work.

References

[1] **Abdel-Salam, M.,** Electric Fields, *in:* **M. Khalifa** (ed.), *High-Voltage Engineering: Theory and Practice*, Dekker, pp. 11-83 (1990).

[2] **Moon, P.** and **Spencer, D.E.,** *Field Theory Handbook: Including Coordinate Systems, Differential Equations and their Solutions*, 2nd ed., Springer-Verlag, Berlin, Germany (1971).

[3] **Digmayer, M., Speck, J.** and **Bohme, H.,** Optimization of multi-electrode-arrangements, *7th Intern. Symposium on High Voltage Engineering, Dresden*, pp. 101-104 (1991).

[4] **Garcia, J.A.** and **Singer, H.,** Contour optimization of high-voltage insulators by means of smoothing cubic spanish, *9th Intern. Symposium on High Voltage Engineering, Graz*, pp. 8343-1-4 (1995).

[5] **Singer, H.** and **Grafoner, P.,** Optimization of electrode and insulator contours, *2nd Proc. International Symposium on High Voltage (ISH), Sept. (1975), Zurich, Switzerland*, pp. 111-116.

[6] **Gronewald, H.,** Computer-aided design of HV insulators, *4th Proc. International Symposium on High Voltage (ISH), No. 11-01, Athens, Greece*, pp. 1-4 (1983).

[7] **Abdel-Salam, M.** and **Stanek, E.K.,** Field optimization of high-voltage insulators, *IEEE Trans. Industry Applications*, **IA-22:** 594-601 (1986).

[8] **Singer, H., Steinbigler, H.** and **Weiss, P.** A charge simulation technique for calculation of high voltage fields, *IEEE Trans. Power Apparatus & System*, **PAS-93:** 1660-1668 (1974).

[9] *FISCHER-products Manual*, Germany, 1976.

[10] **James, M.L., Smith, G.S.** and **Wolford, J.C.,** *Applied Numerical Methods for Digital Computation*, 3rd ed., Harper and Raw Publisher, pp. 149-156 (1985).

[11] **Mukherjee, P.K.** and **Roy, C.K.,** Computation of fields and around insulators by fictitious point charges, *IEEE Trans. Electrical Insulation*, **EI-13:** 24-31 (1978).

[12] **Abramowitz, M.** and **Stegun, I.A.,** *Handbook of Mathematical Functions*, Dover Publ. Inc., New York (1966).

Appendix 1: Electric Potential Equations

$$\phi_1(r,z) = \sum_{j=1}^{N_e+N_c+N_b} \frac{Q(j)}{4\pi\varepsilon_o}\frac{2A}{\pi} + \sum_{J=N_e+N_c+2N_b+N_{t_1}+1}^{N_e+N_c+2N_b+N_t} \frac{Q(j)}{4\pi\varepsilon_o}\frac{2A}{\pi} \tag{1.1}$$

where $A = \dfrac{K(k_1)}{\alpha_1}$

$Q(j)$ is the value of the jth charge in coulombs.

$\alpha_1 = \sqrt{\{r+R(j)\}^2 + \{z-Z(j)\}^2}$

$k_1 = 2\sqrt{\dfrac{rR(j)}{\alpha_1}}$

K is the complete elliptic integral of the first kind[12] and ε_o is the permittivity of free space.

$$\phi_{2o}(r,z) = \sum_{j=1}^{N_e+N_c} \frac{Q(j)}{4\pi\varepsilon_o} + \sum_{J=N_e+N_c+N_b+1}^{N_e+N_c+2N_b} \frac{Q(j)}{4\pi\varepsilon_o}\frac{2A}{\pi} + \sum_{J=N_e+N_c+2N_b+N_{t_1}}^{N_e+N_c+2N_b+N_t} \frac{Q(j)}{4\pi\varepsilon_o}\frac{2A}{\pi} \tag{1.2}$$

$$\phi_{2i}(r,z) = \sum_{j=1}^{N_e+N_c} \frac{Q(j)}{4\pi\varepsilon_o}\frac{2A}{\pi} + \sum_{J=N_e+N_c+N_b+1}^{N_e+N_c+2N_b+N_{t_1}} \frac{Q(j)}{4\pi\varepsilon_o}\frac{2A}{\pi} \tag{1.3}$$

$$\phi_{3ob}(r,z) = \sum_{j=1}^{N_e+N_c} \frac{Q(j)}{4\pi\varepsilon_o}\frac{2A}{\pi} + \sum_{J=N_e+N_c+N_b+1}^{N_e+N_c+2N_b} \frac{Q(j)}{4\pi\varepsilon_o}\frac{2A}{\pi} + \sum_{J=N_e+N_c+2N_b+N_{t_1}+1}^{N_e+N_c+2N_b+N_t} \frac{Q(j)}{4\pi\varepsilon_o}\frac{2A}{\pi} \tag{1.4}$$

$$\phi_{3oa}(r,z) = \sum_{j=1}^{N_e+N_c+N_b} \frac{Q(j)}{4\pi\varepsilon_o}\frac{2A}{\pi} + \sum_{J=N_e+N_c+2N_b+N_{t_1}+1}^{N_e+N_c+2N_b+N_t} \frac{Q(j)}{4\pi\varepsilon_o}\frac{2A}{\pi} \tag{1.5}$$

$$\phi_{3ib}(r,z) = \sum_{j=1}^{N_e+N_c} \frac{Q(j)}{4\pi\varepsilon_o}\frac{2A}{\pi} + \sum_{J=N_e+N_c+N_b+1}^{N_e+N_c+2N_b+N_{t_1}} \frac{Q(j)}{4\pi\varepsilon_o}\frac{2A}{\pi} \tag{1.6}$$

$$\phi_{3ia}(r,z) = \sum_{j=1}^{N_e+N_c+N_b} \frac{Q(j)}{4\pi\varepsilon_o}\frac{2A}{\pi} + \sum_{J=N_e+N_c+2N_b+1}^{N_e+N_c+2N_b+N_{t_1}} \frac{Q(j)}{4\pi\varepsilon_o}\frac{2A}{\pi} \tag{1.7}$$

$$\phi_{4o}(r,z) = \sum_{j=1}^{N_e+N_c+N_b} \frac{Q(j)}{4\pi\varepsilon_o}\frac{2A}{\pi} + \sum_{J=N_e+N_c+2N_b+N_{t_1}}^{N_e+N_c+2N_b+N_t} \frac{Q(j)}{4\pi\varepsilon_o}\frac{2A}{\pi} \tag{1.8}$$

$$\phi_{4i}(r,z) = \sum_{j=1}^{N_e+N_c+N_b} \frac{Q(j)}{4\pi\varepsilon_o}\frac{2A}{\pi} + \sum_{J=N_e+N_c+2N_b+1}^{N_e+N_c+2N_b+N_{t_1}} \frac{Q(j)}{4\pi\varepsilon_o}\frac{2A}{\pi} \tag{1.9}$$

Appendix 2: Normal Electric Field Equations

$$E_{noa}(e,z) = \sum_{j=1}^{N_e+N_c+N_b} \frac{Q(j)}{4\pi\varepsilon_o} B + \sum_{j=N_e+N_c+2N_b+N_{t_1}+1}^{N_e+N_c+2N_b+N_t} \frac{Q(j)}{4\pi\varepsilon_o} B \tag{2.1}$$

where $B = \dfrac{-1}{\pi r} C_1 \sin\alpha - \dfrac{2}{\pi} C_2 \cos\alpha$

α is the inclination angle of the tapered part of the bushing

$$C_1 = \frac{R^2(j) - r^2 + \{z - Z(j)\}^2]\zeta(k_1) - \gamma_1^2 K(k_1)}{\alpha_1 \gamma_1^2}$$

$$C_2 = \frac{\{Z(j) - z\}\zeta(k_1)}{\alpha_1 \gamma_1^2}$$

$$\gamma_1 = \sqrt{\{r - R(j)\}^2 + \{z - Z(j)\}^2}$$

ξ is the complete elliptic integral of the second kind[12].

$$E_{nob}(r,z) = \sum_{j=1}^{N_e+N_c} \frac{Q(j)}{4\pi\varepsilon_o} B + \sum_{j=N_e+N_c+N_b+1}^{N_e+N_c+2N_b} \frac{Q(j)}{4\pi\varepsilon_o} B + \sum_{j=N_e+N_c+2N_b+N_{t1}+1}^{N_e+N_c+2N_b+N_t} \frac{Q(j)}{4\pi\varepsilon_o} B \tag{2.2}$$

$$E_{nia}(r,z) = \sum_{j=1}^{N_e+N_c+N_b} \frac{Q(j)}{4\pi\varepsilon_o} B + \sum_{j=N_e+N_c+2N_b+1}^{N_e+N_c+2N_b+N_{t1}} \frac{Q(j)}{4\pi\varepsilon_o} B \tag{2.3}$$

$$E_{nib}(r,z) = \sum_{j=1}^{N_c+N_t} \frac{Q(j)}{4\pi\varepsilon_o} B + \sum_{j=N_e+N_c+N_b+1}^{N_e+N_c+2N_b+N_{t1}} \frac{Q(j)}{4\pi\varepsilon_o} B \tag{2.4}$$

Appendix 3: Tangential Electric Field Equations

$$E_{toa}(r,z) = \sum_{j=1}^{N_e+N_c+N_b} \frac{Q(j)}{4\pi\varepsilon_o} C + \sum_{j=N_e+N_c+2N_b+N_{t1}+1}^{N_e+N_c+2N_b+N_t} \frac{Q(j)}{4\pi\varepsilon_o} C \tag{3.1}$$

where $C = \dfrac{-1}{\pi r} C_1 \cos\alpha + \dfrac{2}{\pi} C_2 \sin\alpha$

$$E_{tia}(r,z) = \sum_{j=1}^{N_e+N_c+N_b} \frac{Q(j)}{4\pi\varepsilon_o} C + \sum_{j=N_e+N_c+2N_b+1}^{N_e+N_c+2N_b+N_{t1}} \frac{Q(j)}{4\pi\varepsilon_o} C \tag{3.2}$$

أمثـــلة الحقـــول لجـــلب الجهـــد العـــالي

مازن عبد السلام* و أنور مفتي**

* *قسم الهندسة الكهربائية ، جامعة الملك فهد للبترول والمعادن ، الظهران ؛*

** *قسم الهندسة الكهربائية وهندسة الحاسبات ، كلية الهندسة ، جامعة الملك عبد العزيز*
جـــــدة - المملكة العربية السعودية

المستخلص . تم وصف طريقة لأمثلة ضغط الحقول (الكهربائية) على جلب الجهد العالي المتداخلة مع غلاف مؤرض مستو ، وذلك بتعديل الشكل الخارجي للجلبة ، سعيًا وراء توزيع منتظم للحقل المماسي على طول سطح الجلبة . تؤدي هذه الطريقة إلى زيادة جهد الاستهلال للضغط الوميضي السطحي على سطح الجلبة . وقد تم إنجاز عملية الأمثلة الخوارزمية التي جرى تطويرها لغرض حساب المركبة المماسية للحقل على سطح الجلبة . وقد اعتمدت هذه الخوارزمية على طريقة محاكاة الشحنات لاستيفاء الشروط الحدية عند أسطح القطب ، والجلبة ، والغلاف . إن التأثير السائد في عملية الأمثلة يرجع إلى زاوية الميل وارتفاع الجلبة خارج الغلاف .